Published in final edited form as:
J Biomed Opt. 2009 ; 14(4): 044021. doi:10.1117/1.3194142.

Effect of anatomy on spectroscopic detection of cervical dysplasia

Jelena Mirkovic,
Massachusetts Institute of Technology, George R. Harrison Spectroscopy Laboratory, 77 Massachusetts Avenue, Cambridge, Massachusetts 02139

Condon Lau,
Massachusetts Institute of Technology, George R. Harrison Spectroscopy Laboratory, 77 Massachusetts Avenue, Cambridge, Massachusetts 02139

Sasha McGee,
Massachusetts Institute of Technology, George R. Harrison Spectroscopy Laboratory, 77 Massachusetts Avenue, Cambridge, Massachusetts 02139

Chung-Chieh Yu,
Massachusetts Institute of Technology, George R. Harrison Spectroscopy Laboratory, 77 Massachusetts Avenue, Cambridge, Massachusetts 02139

Jonathan Nazemi,
Massachusetts Institute of Technology, George R. Harrison Spectroscopy Laboratory, 77 Massachusetts Avenue, Cambridge, Massachusetts 02139

Luis Galindo,
Massachusetts Institute of Technology, George R. Harrison Spectroscopy Laboratory, 77 Massachusetts Avenue, Cambridge, Massachusetts 02139

Victoria Feng,
Boston Medical Center, Department of Obstetrics and Gynecology, 85 East Concord Street, Boston, Massachusetts 02118

Teresa Darragh,
University of California, San Francisco, Department of Pathology, 1600 Divisadero, Room B618, San Francisco, California 94115

Antonio de las Morenas,
Boston Medical Center, Department of Pathology, 670 Albany Street, Biosquare III Boulevard, Boston, Massachusetts 02118

Christopher Crum,
Brigham and Women's Hospital, Department of Pathology, 75 Francis Street, Boston, Massachusetts 02115

Elizabeth Stier,
Boston Medical Center, Department of Obstetrics and Gynecology, 85 East Concord Street, Boston, Massachusetts 02118

Michael Feld, and

Address all correspondence to: Jelena Mirkovic, George R. Harrison Spectroscopy Laboratory, Massachusetts Institute of Technology, 77 Massachusetts Avenue, Cambridge, MA 02139. Tel: (617) 258-7667; Fax: (617) 253-4513; jedza@mit.edu.

Massachusetts Institute of Technology, George R. Harrison Spectroscopy Laboratory, 77 Massachusetts Avenue, Cambridge, Massachusetts 02139

Kamran Badizadegan
Massachusetts Institute of Technology, George R. Harrison Spectroscopy Laboratory, 77 Massachusetts Avenue, Cambridge, Massachusetts 02139

Abstract

It has long been speculated that underlying variations in tissue anatomy affect *in vivo* spectroscopic measurements. We investigate the effects of cervical anatomy on reflectance and fluorescence spectroscopy to guide the development of a diagnostic algorithm for identifying high-grade squamous intraepithelial lesions (HSILs) free of the confounding effects of anatomy. We use spectroscopy in both contact probe and imaging modes to study patients undergoing either colposcopy or treatment for HSIL. Physical models of light propagation in tissue are used to extract parameters related to tissue morphology and biochemistry. Our results show that the transformation zone, the area in which the vast majority of HSILs are found, is spectroscopically distinct from the adjacent squamous mucosa, and that these anatomical differences can directly influence spectroscopic diagnostic parameters. Specifically, we demonstrate that performance of diagnostic algorithms for identifying HSILs is artificially enhanced when clinically normal squamous sites are included in the statistical analysis of the spectroscopic data. We conclude that underlying differences in tissue anatomy can have a confounding effect on diagnostic spectroscopic parameters and that the common practice of including clinically normal squamous sites in cervical spectroscopy results in artificially improved performance in distinguishing HSILs from clinically suspicious non-HSILs.

Keywords

cervical cancer; squamous intraepithelial lesions; reflectance; fluorescence; quantitative spectroscopy; quantitative spectroscopy imaging

1 Introduction

The effectiveness of reflectance and fluorescence spectroscopy for noninvasive *in vivo* diagnosis of cervical squamous intraepithelial lesions (SILs) has been extensively evaluated. Contact probes, as well as imaging techniques with wide-area surveillance capabilities, have been tested clinically in various stages, from pilot to phase III clinical studies.[1–10] The results show the potential of reflectance and fluorescence spectroscopy, individually or in combination, to improve the effectiveness of disease detection.

The sources of spectroscopic contrast in tissue reflectance and fluorescence due to cervical dysplasia include loss of differentiation of the epithelial cells,[11] degradation and reorganization of stromal collagen by matrix metalloproteinase activity,[12,13] and angiogenesis.[14] Several researchers have developed physically based models to extract tissue spectroscopic parameters and used them to develop disease diagnostic algorithms.[3,7,15–17] The advantage of the model-based spectroscopy techniques is that they provide an understanding of the origins of spectroscopic contrast between normal and diseased tissue, and the diagnosis is based on quantitative information about tissue morphology and biochemistry.

We note that cervical tissue spectroscopy is affected not only by disease, but also by age,[18,19] menopausal status,[19,20] time after the application of acetic acid,[9] and normal variations in cervical anatomy.[2,10,19] For example, spectroscopic differences between normal squamous mucosa (the ectocervix, the outer zone of the cervix) and glandular mucosa (the endocervix, the inner zone of the cervix) have been noted previously[2,10] and explained by differences in

anatomy. Another important source of normal variations in anatomy is the dynamic changes that occur in the cervix during reproductive life, specifically the process of squamous metaplasia in the transformation zone (the region between the ectocervix and the endocervix).[11,21,22]

Although a minority of cervical neoplasia is found in the ectocervix, the vast majority of clinically significant neoplastic lesions (high-grade intraepithelial lesions, HSILs) are found within the transformation zone.[11,22] Normal anatomical variations between the transformation zone and normal squamous mucosa should be reflected in tissue spectroscopy and, if significant, must be accounted for when developing spectral diagnostic algorithms. Furthermore, ectocervix and endocervix are easily identified by colposcopic examination.[23] Therefore, in order to improve the accuracy of clinical HSIL detection, spectroscopy must accurately identify HSILs within the transformation zone. In order to achieve this goal, spectroscopy must be able to reliably resolve the disease process in the context of the background microanatomic complexity inherent in the cervix.

Historically, spectroscopic studies have included clinically normal squamous sites, either nonbiopsied or histopathologically confirmed, in the validation set for diagnosing HSILs.[2,4,6,8,10] Mourant et al.[7] and Georgakoudi et al.[3] noted an apparent increase in diagnostic power when clinically normal tissues were included in the validation set. Georgakoudi et al. also noted that normal squamous tissue and the transformation zone had different spectroscopic properties, consistent with the Freeberg et al.[19] observation that tissue type influences both reflectance and fluorescence measurements. Freeberg et al. concluded that understanding the effects of anatomy on spectroscopy may have a significant impact on diagnostic algorithm development. Nevertheless, this has not been further explored, and the reasons for differences in diagnostic power when clinically normal tissues were included have not been explained.

In this study, we demonstrate the effects of cervical anatomy on spectroscopy with an aim to facilitate the development of a diagnostic algorithm free of the confounding effects of cervical anatomy. We use spectroscopy in both contact probe and imaging modes to study patients undergoing either colposcopic examination or treatment via the loop electrosurgical excision procedure (LEEP) for uterine cervical squamous neoplasia. Physical models are used to fit the spectra and extract parameters related to tissue morphology and biochemistry. The extracted parameters are then used to develop spectroscopic algorithms with two aims: (1) to characterize changes in spectroscopic parameters due to anatomy, and (2) to examine the effects of anatomy on the apparent performance of diagnostic algorithms for identifying HSILs.

2 Materials and Methods

2.1 Data Collection

The clinical *in vivo* study was conducted at the Boston Medical Center (BMC). The protocol was approved by the BMC Institutional Review Board, as well as the Committee on the Use of Humans as Experimental Subjects of the Massachusetts Institute of Technology.

The contact probe study involved 43 patients undergoing colposcopic evaluation following an abnormal Pap smear. For each patient, reflectance and fluorescence spectra were collected from a clinically normal squamous (CNS) site as well as abnormal sites using a fiber-optic-based clinical device developed by our laboratory known as the fast excitation emission matrix (FastEEM). The instrument and the calibration procedures have been previously described.[24] The optical fiber probe, which samples an area of tissue ~1 mm in diameter, was disinfected with CIDEX OPA (Advanced Sterilization Products, Irvine, California) before each procedure. After the application of acetic acid (5% solution) to the cervix during colposcopy, the probe was brought into gentle contact with the tissue. Each measurement, which consisted of the

average of five sets of white-light reflectance spectra (300 to 800-nm emission) and five sets of nine fluorescence spectra (308 460-nm excitation), was acquired in approximately 3 seconds. Two to three measurements were acquired for each tissue site. Colposcopically abnormal sites were then biopsied and evaluated by histopathology. Clinically normal sites were not biopsied.

The contact probe study was extended to the imaging mode using a new technique, quantitative spectroscopy imaging (QSI).[25] *In vivo* imaging data were acquired using the QSI device from two patients who were referred for LEEP due to prior abnormal biopsy results. For each patient, reflectance and fluorescence spectra from the entire cervix were obtained. QSI illuminates a 1-mm^2 region of the cervix with visible and 337-nm fluorescence excitation light and collects reflectance and fluorescence spectra. Once the measurement for one region is completed, another 1-mm^2 region is interrogated via raster scanning until a 2.1 cm×2.1 cm area of the cervix with 441 interrogation points (pixels) is examined.

2.2 Histopathology

Each contact probe biopsy specimen underwent standard histopathology processing. The hematoxylin and eosin stained tissue sections were evaluated by three experienced pathologists using standard diagnostic criteria (C.C., A.M., T.D.). Consensus diagnosis (agreement of two of the three pathologists) was used as the diagnostic gold standard. Each biopsied site was classified as either HSIL or biopsied non-HSIL (negative for SIL or low-grade squamous intraepithelial lesion, LSIL). All sites were further examined by a single pathologist (C.C.) for the absence or presence of features consistent with the transformation zone.

Upon submission to pathology, the two LEEP specimens studied by imaging instrument were cut into 12 pieces corresponding to the 12 clock directions per standard of care. From each piece, a section extending from endocervix through the transformation zone to ectocervix was prepared for evaluation under a microscope. For each section, a single pathologist recorded the extent and location of any HSIL present with millimeter precision. The location and the extent of the endocervix, transformation zone, and ectocervix were also recorded. The end result was a combined anatomy/disease map showing the location of cervical tissue zones, as well as the location of HSIL on the cervix.

2.3 Data Analysis

2.3.1 Contact probe—The results from four patients were excluded due to instrument malfunctions (e.g., CCD camera overheat, probe damage). Raw spectra for each set of measurements were examined, and those with poor overlap between repeat measurements were excluded. We excluded three study sites for which all sets in a measurement were inconsistent (>10% average standard deviation between measurements) as well as four sites for which the tissue started bleeding due to probe contact.

2.3.2 Diffuse reflectance spectroscopy (DRS)—The reflectance spectra were analyzed using the diffusion approximation model developed by Zonios et al.[26] to extract properties such as the reduced scattering coefficient, μ_s' and the absorption coefficient, μ_a. An analytical expression was used to describe μ_s';

$$\mu_s'(\lambda)=A\left(\frac{\lambda}{\lambda_0}\right)^{-B}+C\left(\frac{\lambda}{\lambda_0}\right)^{-4}\ [\mathrm{mm}^{-1}], \tag{1}$$

where the wavelength, λ, is expressed in units of microns, and λ_0 is equal to 0.7 μm. The *A* parameter is related to scatterer density, and the *B* parameter is related to the size of the Mie scatterers. The first term on the right-hand side of this expression has been commonly used by other researchers to model scattering from cells and tissues. We found that the second term was required to accurately model reflectance at shorter wavelengths (<400 nm), in which scattering from Rayleigh particles is significant. Reflectance spectra were fit over the range of 350 to 750 nm using a constrained nonlinear least-squares fitting algorithm.

The absorption coefficient was modeled as the sum of the hemoglobin and β-carotene absorption coefficients as follows:

$$\mu_a(\lambda)=\mu_a^{Hb}(\lambda)+\mu_a^{\beta-car}(\lambda)\,[\mathrm{mm}^{-1}]. \tag{2}$$

The absorption coefficient of hemoglobin was modified by a correction factor to account for the fact that hemoglobin is confined to blood vessels, rather than homogeneously distributed in the tissue.[27] This effect, called *vessel packaging*, is caused by the fact that blood vessels are opaque to 420 nm light, which is strongly absorbed by hemoglobin, but become more transparent to longer wavelengths of light. As a result, the intensity of the Soret band (420 nm) is reduced relative to that of the weaker hemoglobin absorption bands. We used the correction factor $C_{diff}(\lambda,bvr)$ developed by van Veen et al.[28] and Svaasand et al.[29] to account for the effects of vessel packaging:

$$c_{diff}(\lambda)=\left\{\frac{1-\exp[-2\cdot\mu_a^{blood}(\lambda)\cdot bvr]}{2\cdot\mu_a^{blood}(\lambda)\cdot bvr}\right\}, \tag{3}$$

where *bvr is* the effective blood vessel radius in units of mm, and $\mu_a^{blood}(\lambda)$ is the absorption coefficient of whole blood in units of mm^{-1}, given by:

$$\mu_a^{blood}(\lambda)=\log 10\cdot 150\,\mathrm{mg/mL}\cdot[(1-\alpha)\varepsilon_{Hb}(\lambda)+\alpha\varepsilon_{HbO_2}(\lambda)], \tag{4}$$

where α is the oxygen saturation of hemoglobin, and ε_{HbO2} and ε_{Hb} are the well-known extinction coefficients of oxygenated and deoxygenated hemoglobin.[30] We assume that the hemoglobin concentration of whole blood is 150 mg/mL (Ref. [28]), and impose a lower limit of 2.5 μm for *bvr*, since the minimum diameter of a capillary is on the order of 5 to 7 μm.[31] The absorption coefficient of hemoglobin, μ_a^{Hb}, is then given by the expression:

$$\mu_a^{Hb}(\lambda)=C_{diff}(\lambda)\cdot\nu\cdot\mu_a^{blood}(\lambda)\,[\mathrm{mm}^{-1}], \tag{5}$$

where *v* is the volume fraction of blood sampled and is described by the ratio:

$$\nu=[Hb]/150, \tag{6}$$

with *Hb* the total concentration of hemoglobin in units of mg/mL.

The absorption coefficient of β-carotene, $\mu_a^{\beta-car}$, is given by:

$$\mu_a^{\beta-car}(\lambda)=\log 10 \cdot [\beta - car] \cdot \varepsilon_{\beta-car}(\lambda), \quad (7)$$

where [β-*car*] is the concentration of β-carotene in mg/ml, and $\varepsilon_{\beta\text{-}car}$ is its extinction coefficient.[32] Although β-carotene has not been previously used in modeling reflectance measurements of the cervix, there are numerous reports in the literature of its presence in cervical cells as well as in plasma.[33,34]

2.3.3 Intrinsic fluorescence spectroscopy (IFS)—An intrinsic fluorescence algorithm based on the photon-migration model was used to correct the tissue fluorescence emission spectra for distortions introduced by absorption and scattering.[14] The intrinsic fluorescence spectra were fit using a linear combination of tissue fluorophore basis spectra. The tissue fluorophore basis spectra were extracted from the intrinsic fluorescence spectra using multivariate curve resolution (MCR).[35] The areas under the IFS spectra, as well as the basis spectra, were normalized to unity. We focus the analysis to IFS excited at 340 nm, an excitation wavelength available for both the contact probe system and the imaging system. For 340-nm excitation, the intrinsic fluorescence emission spectra could be accurately modeled as a linear combination of two fluorophores, the reduced form of nicotinamide adenine dinucleotide (NADH) and collagen (Coll). The IFS spectra were fit to extract the fractional contribution of these two components.

2.3.4 Spectroscopy parameters—Using the DRS and IFS models described earlier, we obtained nine parameters from modeling contact probe tissue reflectance and fluorescence: *A* [mm^{-1}], *B*, *C* [mm^{-1}], *Hb* [mg/ml], α, *bvr* [mm], β-*car* [mg/ml], *Coll*, and *NADH*. These nine parameters were used in the development and statistical analysis of the diagnostic algorithms as described in the following.

2.3.5 Imaging data analysis—The same DRS and IFS analysis applied to the contact probe data was also applied to the imaging data. Unlike the contact probe data, which extends to the ultraviolet (UV) region, the imaging instrument collects reflectance spectra only over the visible wavelength range. Reflectance spectra were fit over the range of 400 to 700 nm using a constrained nonlinear least-squares fitting algorithm. For this wavelength range, the analysis of the reflectance spectra did not require inclusion of the *C* parameter or *bvr*. Additionally, reflectance data collected with the imaging instrument did not demonstrate the absorption features of β-carotene. The output of the imaging data analysis is 21×21 parameter maps for each of the six parameters: *A* [mm−1], *B*, [*Hb*] [mg/ml], α, *Coll*, and *NADH*.

2.3.6 Development and testing of spectroscopic algorithms—We studied spectroscopic parameters from different zones of the cervix, using both contact probe and imaging modes. Tissue parameters were correlated with histopathology diagnosis for all data collected from the imaging patients and clinically suspicious sites from the probe data set. In the case of contact probe CNS sites, tissue parameters were correlated with clinical impression. A two-sided Wilcoxon rank sum test was used to test the hypothesis that the extracted spectroscopic parameter distributions of different tissue zones or different groups of sites were different. A *p*-value of < 0.05 was considered significant. The spectral algorithms were developed by using logistic regression models to identify the significant spectroscopic parameters providing the diagnostic information. The likelihood ratio test was used to assess the significance of each of the spectroscopic parameters in the logistic regression model.[36] A *p*-value <0.05 was considered to be significant. Leave-one-out cross-validation (LCV) was used to construct receiver-operator characteristic (ROC) curves for the spectral algorithms. The ROC curve is a plot of sensitivity (true-positive rate) against 1-specificity (false-positive

rate) for a range of cutoff points (probability thresholds). The discrimination ability was evaluated by the area under the ROC curve (AUC), as well as the sensitivity and specificity. The AUC represents the overall accuracy of the model across the entire range of thresholds. Perfect separation is characterized by an AUC value of 1, and the inability to differentiate between two groups is characterized by an AUC value of 0.5. In the following, we report a point on the ROC curve that is the shortest distance away from the point of perfect separation (100% sensitivity and 100% specificity), defined by:

$$\min\left[\left(1-\frac{sensitivity}{100}\right)^2+\left(1-\frac{specificity}{100}\right)^2\right]^{1/2}. \quad (8)$$

We refer to this point whenever we quote sensitivity and specificity values.

To examine the impact of including CNS sites in the validation set, we constructed and tested five data sets with varying percentages of CNS sites. For each percentage of CNS sites, we determined the significant parameters that differentiate HSIL sites from everything else (biopsied non-HSILs and CNS). In order to evaluate the discrimination ability based on absorption, scattering, and fluorescence separately, we first tested a logistic regression algorithm based on each of the parameters alone. Next, we developed a logistic regression model based on a combination of significant spectroscopic parameters providing the highest diagnostic power.

3 Results

3.1 Data Set

As shown in Table 1, our contact probe data set consisted of 33 CNS sites and 51 clinically suspicious biopsied sites, out of which 30 were negative for SIL, 12 were LSIL, and 9 were HSIL. For the purposes of developing a diagnostic algorithm that aims to detect the clinically significant HSIL sites, the sites evaluated on histology as negative for SIL and the LSIL sites were combined as biopsied non-HSIL. We emphasize that these biopsied non-HSIL sites do not include the 33 CNS sites. The imaging data was collected from two LEEP patients, which were entirely free of HSIL by histopathology. Imaging data provided 51 additional normal squamous (NS) sites and 45 additional normal transformation zone (NT) sites, representing all analyzable data in these two categories.

3.2 Microscopic Characterization

Histopathology evaluation confirmed that 36 of 51 contact probe biopsied sites were from the transformation zone. Fifteen sites could not be histologically confirmed as transformation zone (e.g., stroma was not visible on the histology slides to ensure full assessment, or glandular elements were not present). All of the HSIL sites except one for which stroma was not visible were confirmed to be from the transformation zone.

3.3 Normal Squamous Mucosa and Normal Transformation Zone Are Spectrally Different

3.3.1 Contact probe results—In order to determine the spectroscopic differences between the transformation zone and normal squamous mucosa, we compared histologically confirmed normal transformation zone (NT) sites with the CNS sites. Our data set consisted of 20 NT sites that showed no evidence of dysplasia. Based on the Wilcoxon rank sum test, the majority of the extracted spectroscopic parameters were significantly different between the CNS and NT sites. Compared to the NT sites, the CNS sites exhibited significantly higher values of *Coll* and *A*, and lower values of *C*, *Hb*, *α*, *β-car*, and *bυr*. When logistic regression and LCV

were performed, CNS could be differentiated from NT based on *Coll* and *Hb* with an AUC, sensitivity, and specificity of 0.87, 90%, and 73%, respectively. The contribution of other parameters was negligible. The box plots of the three most significant parameters, *A*, *Hb*, and *Coll*, as well as the ROC curve for differentiating CNS from NT, are shown in Fig. 1.

3.3.2 Imaging results—In order to ensure that the results shown in Fig. 1 were not strictly due to clinically suspicious nature of contact probe NT sites, we used imaging data to perform the same comparison. Based on the Wilcoxon rank sum test, all extracted reflectance and fluorescence parameters were significantly different between the NS and NT sites. Just as in the case of the contact probe data, the NS sites exhibited significantly higher values of *Coll* and *A* and lower values of *Hb* and α than NT sites. Additionally, NS sites exhibited higher values of the *B* parameter than for the NT sites. When logistic regression and LCV were performed, CNS could be differentiated from NT based on *Coll* and *Hb*, with an AUC, sensitivity, and specificity of 0.98, 98%, and 98%, respectively. The box plots of the three most significant parameters, *A*, *Hb*, and *Coll*, as well as the ROC curve for the logistic regression model for differentiating the NS from the NT sites using imaging data, are shown in Fig. 2.

3.4 Normal Squamous Mucosa and HSIL Are Spectrally Different Due to Anatomy Differences

As we have shown in the previous section, normal anatomical variations are reflected in tissue spectroscopy. To determine whether normal variations in anatomy impact spectroscopy differences between normal squamous mucosa and HSIL, the vast majority of which are found in the transformation zone, we investigated the spectral difference between CNS and biopsied non-HSIL and HSIL. Based on the Wilcoxon rank sum test, a majority of the extracted parameters were significantly different for CNS and biopsied non-HSIL, as well as HSIL. Just as in the case of CNS versus NT, the CNS sites exhibited higher values of *Coll* and *A* and lower values of *C*, *Hb*, α, and $b\sigma r$ than both biopsied non-HSIL and HSIL sites. When logistic regression and LCV were performed, biopsied non-HSIL sites could be differentiated from CNS using *Coll* and *Hb*, with an AUC, sensitivity, and specificity of 0.88, 81%, and 85%, respectively. With these same parameters, HSIL sites could be differentiated from CNS with an AUC, sensitivity, and specificity of 0.92, 89%, and 97%, respectively. Box plots for the three most significant parameters, *A*, *Coll*, and *Hb*, are shown in Figs 3(a) –3(c), respectively. The corresponding ROC plots are shown in Fig. 3(d).

3.5 Diagnostic Performance for HSIL Detection Is A Function of the Percentage of CNS Sites Included in the Validation Set

To quantify the effect of including CNS sites in the validation set on diagnostic performance for identifying HSIL, we constructed and tested five data sets with varying percentages of CNS sites. For each data set, we used the same nine HSIL sites as the positive group, while the negative group contained percentages of CNS sites ranging from 0 to 100%, randomly selected from all CNS sites, as shown in Table 2.

For each data set, we first determined the significant parameters for differentiating the positive (HSIL) group from the negative (biopsied non-HSIL and CNS) group using the Wilcoxon rank sum test. As shown in Table 2, non-HSIL sites (0% CNS group) can be differentiated from HSIL by *A*, *Hb*, and *Coll* parameters. As the percentage of CNS in the negative group increased, the number of significant parameters increased. All spectroscopic parameters except β-carotene were significantly different when the negative group consisted only of CNS sites.

We then calculated the AUC for the logistic regression model based on each of the significant parameters separately, and finally for the combination of parameters that produced the best diagnostic performance. For each data set, a combination of *Coll* and *Hb* provided the best diagnostic performance. For the individual parameters (Fig. 4), as well as the combination

providing the best diagnostic performance, the AUC increased as the percentage of CNS increased.

4 Discussion

Although the potential confounding effect of anatomical variations on spectroscopic diagnostic algorithms have long been suspected,[3,19] these effects have never been formally examined. Specifically, in spite of known spectroscopic differences between normal squamous mucosa and transformation zone, these anatomically different tissue sites have been historically combined during development of diagnostic algorithms for cervical neoplasia.[2,4,6,8,10] In this paper, we demonstrate that combining anatomically different sites into the diagnostic algorithm will result in higher than clinically relevant levels of diagnostic performance.

The results from the contact probe (Fig. 1) and imaging studies (Fig. 2) demonstrated that the transformation zone is spectroscopically distinct from the normal squamous mucosa. Regardless of the clinical impression (suspicious versus not), no differences in the parameter trends were observed, confirming that the spectroscopic differences are related to anatomy and not clinical impression. Both contact probe and imaging data demonstrated that NT sites exhibit lower values of *Coll* and *A* and higher values of *Hb* compared to the normal squamous sites. These findings are consistent with the transformation zone comprising both squamous and glandular features. Higher hemoglobin concentration for NT sites compared to normal squamous sites could be explained by the fact that the normal squamous mucosa is covered by stratified squamous epithelium, while in the glandular mucosa, small capillary loops are located directly beneath the single layer of mucus-secreting columnar cells. The lower scattering within NT is likely related to less stromal collagen fibers than in the squamous mucosa. The same anatomical difference may explain the lower collagen fluorescence in NT compared to squamous mucosa. Thus, normal squamous mucosa is anatomically and spectroscopically different from the transformation zone (comprising both squamous and glandular features), even in the absence of clinical and histological abnormality.

CNS sites are spectroscopically distinct from the transformation zone, and the same parameters that distinguish CNS from transformation zone also separate CNS from HSIL (Fig. 3). These findings indicate that the spectral differences seen between normal squamous and HSIL sites are largely due to anatomical differences between normal squamous mucosa and the transformation zone, and not due to a disease state. These findings also explain why Mourant et al.[7] and Georgakoudi et al.[3] saw an improvement in diagnostic performance for dysplasia when CNS was included in their analysis. Similarly, other studies including clinically normal squamous sites (biopsied or not) in the analysis may have reported higher levels of performance than clinically relevant.[2,4,6,8,10]

We further demonstrate that the magnitude of the confounding effect is directly proportional to the percentage of CNS sites included in the validation (Fig. 4). We find that as the percentage of CNS in the negative group decreases, the number of significant parameters differentiating HSIL from everything else also decreases (Table 2). The data demonstrate that the confounding influence of including CNS affects not only the performance levels but also the number of specific spectroscopic parameters that can be used in the diagnostic algorithm. The affected parameters include those describing the scattering, absorption, and fluorescence properties of tissue.

5 Conclusions

Normal transformation zone is anatomically, histologically, and spectroscopically different from the normal squamous mucosa. As the vast majority of the HSILs are found in the

transformation zone, the spectral differences between normal squamous mucosa and HSIL are largely due to normal anatomical differences. Based on our findings, including clinically normal squamous sites into the data set that is used to develop or evaluate the performance of the algorithm for detection of HSIL is a confounding artifact that artificially increases performance values with respect to the key differentiation to be made—namely, distinguishing HSILs from clinically suspicious non-HSILs. In order to properly evaluate the accuracy of clinical disease detection, spectroscopic data must be analyzed within the appropriate anatomical context. This becomes a critical issue for wide-area imaging, where data must be appropriately processed to account for underlying normal anatomical variations. The importance of considering anatomy likely applies to other organs and disease states and requires further investigation.

Acknowledgments

This research was funded by National Institutes of Health Grant No. CA097966 and the Laser Biomedical Research Center Grant No. P41 RR02594.

References

1. Alvarez RD, Wright TC. Optical Detection Group. Effective cervical neoplasia detection with a novel optical detection system: a randomized trial. Gynecol Oncol 2007;104(2):281–289. [PubMed: 17173959]
2. Chang SK, Mirabal YN, Atkinson EN, Cox D, Malpica A, Follen M, Richards-Kortum R. Combined reflectance and fluorescence spectroscopy for *in vivo* detection of cervical pre-cancer. J Biomed Opt 2005;10(2):024031. [PubMed: 15910104]
3. Georgakoudi I, Sheets EE, Muller MG, Backman V, Crum CP, Badizadegan K, Dasari RR, Feld MS. Trimodal spectroscopy for the detection and characterization of cervical precancers *in vivo*. Am J Obstet Gynecol 2002;186(3):374–382. [PubMed: 11904594]
4. Huh WK, Cestero RM, Garcia FA, Gold MA, Guido RS, McIntyre-Seltman K, Harper DM, Burke L, Sum ST, Flewelling RF, Alvarez RD. Optical detection of high-grade cervical intraepithelial neoplasia *in vivo*: results of a 604-patient study. Am J Obstet Gynecol 2004;190(5):1249–1257. [PubMed: 15167826]
5. Marin NM, Milbourne A, Rhodes H, Ehlen T, Miller D, Benedet L, Richards-Kortum R, Follen M. Diffuse reflectance patterns in cervical spectroscopy. Gynecol Oncol 2005;99(3):S116–S120. [PubMed: 16165197]
6. Mirabal YN, Chang SK, Atkinson EN, Malpica A, Follen M, Richards-Kortum R. Reflectance spectroscopy for *in vivo* detection of cervical precancer. J Biomed Opt 2002;7(4):587–594. [PubMed: 12421125]
7. Mourant JR, Bocklage TJ, Powers TM, Greene HM, Bullock KL, Marr-Lyon LR, Dorin MH, Waxman AG, Zsemlye MM, Smith HO. *In vivo* light scattering measurements for detection of precancerous conditions of the cervix. Gynecol Oncol 2007;105(2):439–445. [PubMed: 17303229]
8. Nordstrom RJ, Burke L, Niloff JM, Myrtle JF. Identification of cervical intraepithelial neoplasia (CIN) using UV-excited fluorescence and diffuse-reflectance tissue spectroscopy. Lasers Surg Med 2001;29 (2):118–127. [PubMed: 11553898]
9. Orfanoudaki IM, Themelis GC, Sifakis SK, Fragouli DH, Panayiotides JG, Vazgiouraki EM, Koumantakis EE. A clinical study of optical biopsy of the uterine cervix using a multispectral imaging system. Lasers Surg Med 2005;96(1):119–131.
10. Ramanujam N, Mitchell MF, Mahadevan A, Thomsen S, Malpica A, Wright T, Atkinson N, RichardsKortum R. Development of a multivariate statistical algorithm to analyze human cervical tissue fluorescence spectra acquired *in vivo*. Lasers Surg Med 1996;19(1):46–62. [PubMed: 8836996]
11. Blaustein, A.; Kurman, RJ. Blaustein's Pathology of the Female Genital Tract. Springer; New York: 2002.
12. Kalluri R, Zeisberg M. Fibroblasts in cancer. Nat Rev Cancer 2006;6(5):392–401. [PubMed: 16572188]

13. Nagase H, Woessner JF. Matrix metalloproteinases. J Biol Chem 1999;274(31):21491–21494. [PubMed: 10419448]
14. Mazibrada J, Ritta M, Mondini M, De Andrea M, Azzimonti B, Borgogna C, Ciotti M, Orlando A, Surico N, Chiusa L, Landolfo S, Garigho M. Interaction between inflammation and angiogenesis during different stages of cervical carcinogenesis. Gynecol Oncol 2008;108(1):112–120. [PubMed: 17936343]
15. Chang SK, Marin N, Follen M, Richards-Kortum R. Model-based analysis of clinical fluorescence spectroscopy for *in vivo* detection of cervical intraepithelial dysplasia. J Biomed Opt 2006;11(2): 024008. [PubMed: 16674198]
16. Weber CR, Schwarz RA, Atkinson EN, Cox DD, MacAulay C, Follen M, Richards-Kortum R. Model-based analysis of reflectance and fluorescence spectra for *in vivo* detection of cervical dysplasia and cancer. J Biomed Opt 2008;13(6):064016. [PubMed: 19123662]
17. Mourant JR, Powers TM, Bocklage TJ, Greene HM, Dorin MH, Waxman AG, Zsemlye MM, Smith HO. *In vivo* light scattering for the detection of cancerous and precancerous lesions of the cervix. Appl Opt 2009;48(10):D26–D35. [PubMed: 19340117]
18. Brookner CK, Follen M, Boiko I, Galvan J, Thomsen S, Malpica A, Suzuki S, Lotan R, Richards-Kortum R. Autofluorescence patterns in short-term cultures of normal cervical tissue. Photochem Photobiol 2000;71(6):730–736. [PubMed: 10857369]
19. Freeberg JA, Serachitopol DM, McKinnon N, Price R, Atkinson EN, Cox DD, MacAulay C, Richards-Korturn R, Follen M. Fluorescence and reflectance device variability throughout the progression of a phase II clinical trial to detect and screen for cervical neoplasia using a fiber optic probe. J Biomed Opt 2007;12(3):034015. [PubMed: 17614723]
20. Gill EM, Malpica A, Alford RE, Nath AR, Follen M, Richards-Kortum RR, Ramanujam N. Relationship between collagen autofluorescence of the human cervix and menopausal status. Photochem Photobiol 2003;77(6):653–658. [PubMed: 12870852]
21. Kumar, V.; Abbas, AK.; Fausto, N.; Robbins, SL.; Cotran, RS. Robbins and Cotran Pathologic Basis of Disease. Elsevier Saunders; Philadelphia: 2005.
22. Crum, CP. Diagnostic Gynecologic, and Obstetrics Pathology. Elsevier Saunders; Philadelphia: 2006.
23. Ferris, DG. Modern Colposcopy: Textbook and Atlas. Kendall/Hunt; Dubuque, Iowa: 2004.
24. Tunnell JW, Desjardins AE, Galindo L, Georgakoudi I, McGee SA, Mirkovic J, Mueller MG, Nazemi J, Nguyen FT, Wax A, Zhang QG, Dasari RR, Feld MS. Instrumentation for multi-modal spectroscopic diagnosis of epithelial dysplasia. Technol Cancer Res Treat 2003;2(6):505–514. [PubMed: 14640762]
25. Yu CC, Lau C, O'Donoghue G, Mirkovic J, McGee S, Galindo L, Elackattu A, Stier E, Grillone G, Badizadegan K, Dasari RR, Feld MS. Quantitative spectroscopic imaging for non-invasive early cancer detection. Opt Express 2008;16(20):16227–16239. [PubMed: 18825262]
26. Zonios G, Perelman LT, Backman VM, Manoharan R, Fitzmaurice M, Van Dam J, Gundam MS. *In vivo* light scattering for the detection of cancerous and precancerous lesions of the cervix. Appl Opt 1999;38(31):6628–6637. [PubMed: 18324198]
27. Lau C, Scepanovic O, Mirkovic J, McGee S, Yu C-C, Fulghum S Jr, Wallace M, Tunnell J, Bechtel K, Feld MS. Reevaluation of model-based LSS for tissue spectroscopy. J Biomed Opt 2009;14(2): 024031. [PubMed: 19405760]
28. van Veen RLP, Verkruysse W, Sterenborg HJCM. Diffuse-reflectance spectroscopy from 500 to 1060 nm by correction for inhomogeneously distributed absorbers. Opt Lett 2002;27(4):246–248. [PubMed: 18007768]
29. Svaasand LO, Fiskerstrand EJ, Kopstad G, Norvang LT, Svaasand EK, Nelson JS, Berns MW. Therapeutic response during pulsed laser treatment of port-wine stains: dependence on vessel diameter and depth in dermis. Lasers Med Sci 1995;10(4):235–243.
30. Prahl, SA. Optical absorption of hemoglobin. Oregon Medical Laser Center; 1999. http://omlc.ogi.edu/spectra/hemoglobin/index.html
31. Best, CH.; Taylor, NB.; West, JB. Best and Taylor's Physiological Basis of Medical Practice. Williams & Wilkins; Baltimore: 1991.
32. Du H, Fuh RCA, Li JZ, Corkan LA, Lindsey JS. PhotochemCAD: a computer-aided design and research tool in photochemistry. Photochem Photobiol 1998;68(2):141–142.

33. Palan PR, Mikhail MS, Basu J, Romney SL. Beta-carotene levels in exfoliated cervicovaginal epithelial-cells in cervical intraepithelial neoplasia and cervical-cancer. Am J Obstet Gynecol 1992;167(6):1899–1903. [PubMed: 1471714]

34. Palan PR, Mikhail MS, Basu J, Romney SL. Plasma-levels of antioxidant beta-carotene and alpha-tocopherol in uterine cervix dysplasias and cancer. Nutr Cancer 1991;15(1):13–20. [PubMed: 2017395]

35. Muller MG, Valdez TA, Georgakoudi I, Backman V, Fuentes C, Kabani S, Laver N, Wang ZM, Boone CW, Dasari RR, Shapshay SM, Feld MS. Spectroscopic detection and evaluation of morphologic and biochemical changes in early human oral carcinoma. Cancer 2003;97(7):1681–1692. [PubMed: 12655525]

36. Kleinbaum, DG. Logistic Regression: A Self-Learning Text. Springer; New York: 1994.

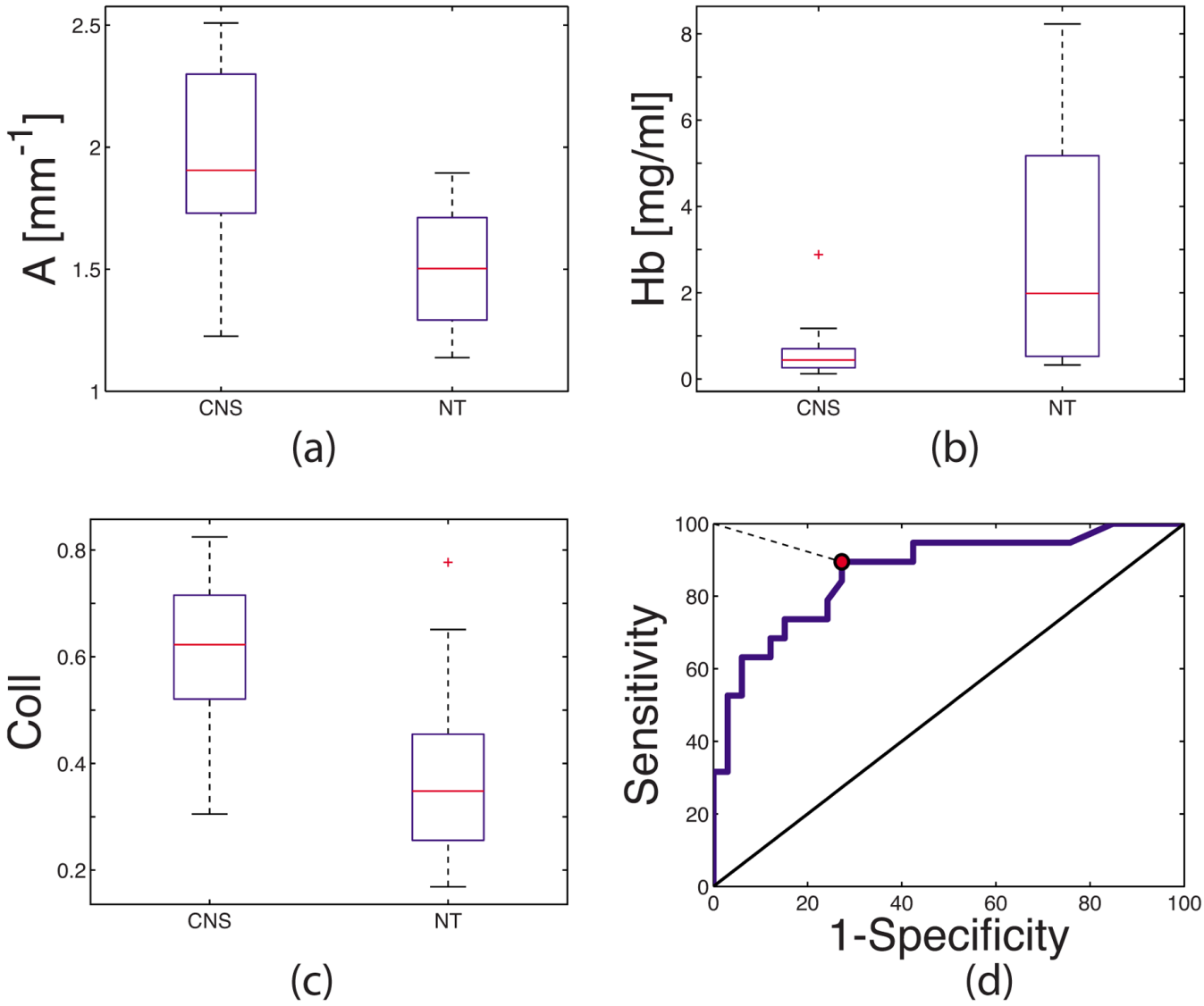

Fig. 1.

Discrimination of CNS from NT using contact probe data. Box plots of: (a) *A* parameter (mm^{-1}); (b) hemoglobin concentration (*Hb*), (mg/ml); (c) fraction of IFS due to collagen (*Coll*); (d) LCV ROC plot for the logistic regression algorithm differentiating CNS from NT based on *Coll* and *Hb*: ROC curve (solid line), the 45-deg line (AUC=0.5), the point of representative sensitivity/specificity (circle), and the shortest distance from the point of perfect separation (dashed line). Box plots: median (horizontal line within the box), upper and lower quartiles (upper and lower edges of the box, respectively), extent of the data (whiskers), and outliers (crosses, data points that are more than 1.5 times the interquartile range below the lower quartile or above the upper quartile).

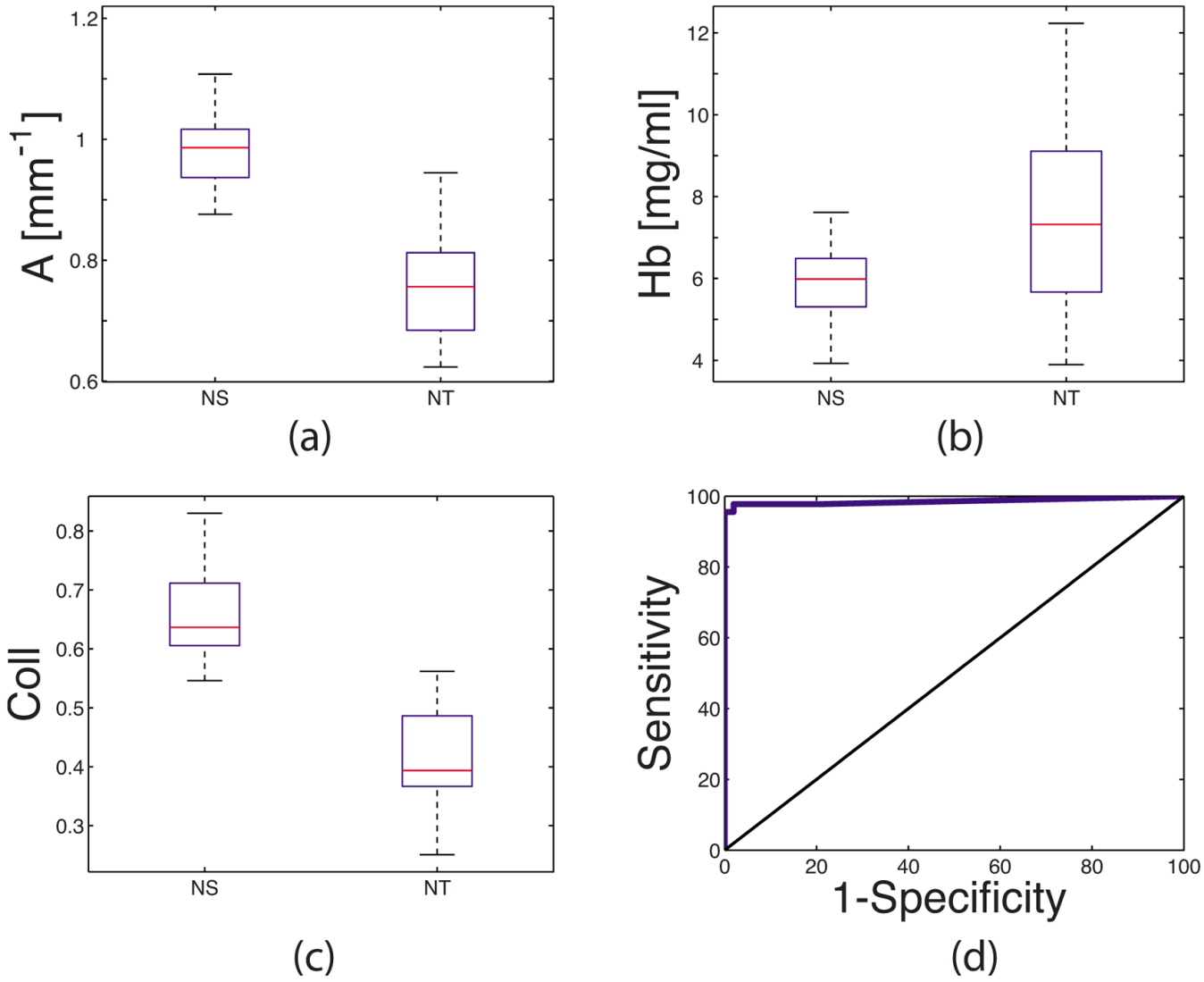

Fig. 2.

Discrimination of CNS from NT using imaging data. Box plots of (a) *A* parameter, (b) *Hb*, (c) *Coll* (same units as in Fig. 1), and (d) LCV ROC curve for the logistic regression algorithm based on *Coll* and *Hb* for differentiating CNS from NT sites: ROC curve (solid line) and the 45-deg line (AUC=0.5).

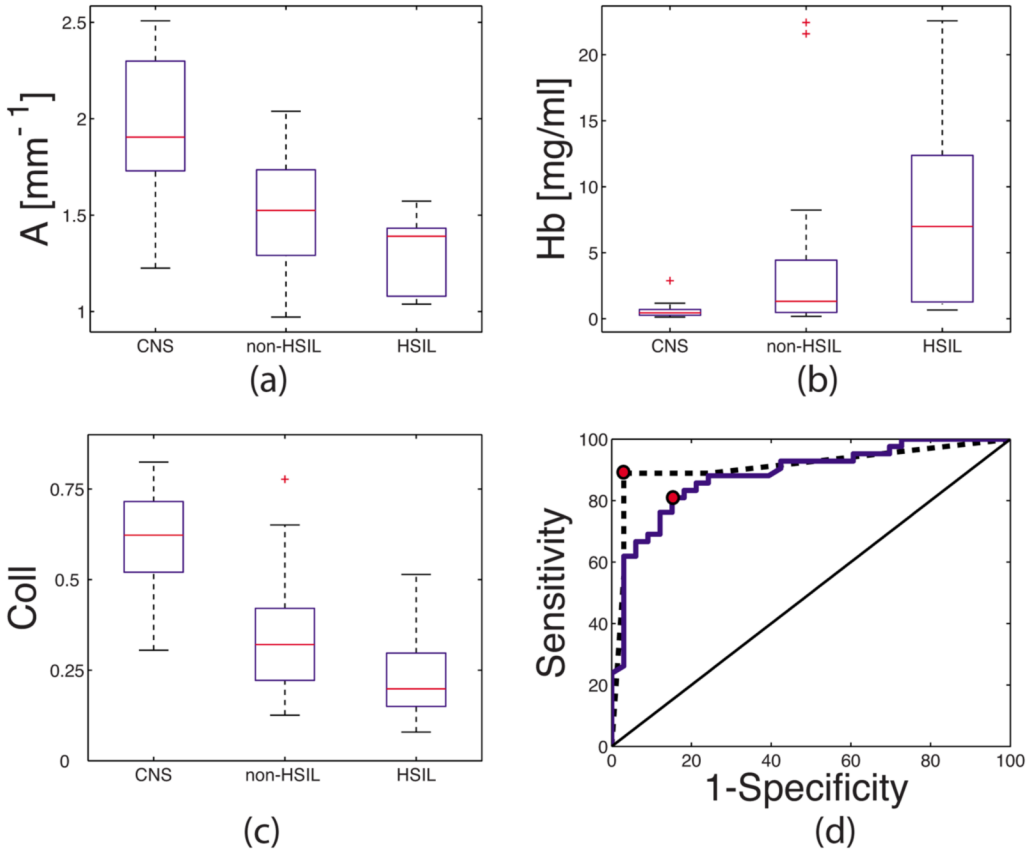

Fig. 3.

Discrimination of CNS from HSIL and non-HSIL. Box plots of (a) *A* parameter, (b) *Hb*, (c) *Coll* (same units as in Fig. 1), and (d) LCV ROC curve for the logistic regression algorithm based on *Coll* and *Hb* for differentiating CNS sites from HSIL sites (dashed line), and CNS sites from non-HSIL sites (solid line), the 45-deg line (AUC=0.5), and the points of representative sensitivity/specificity (circles).

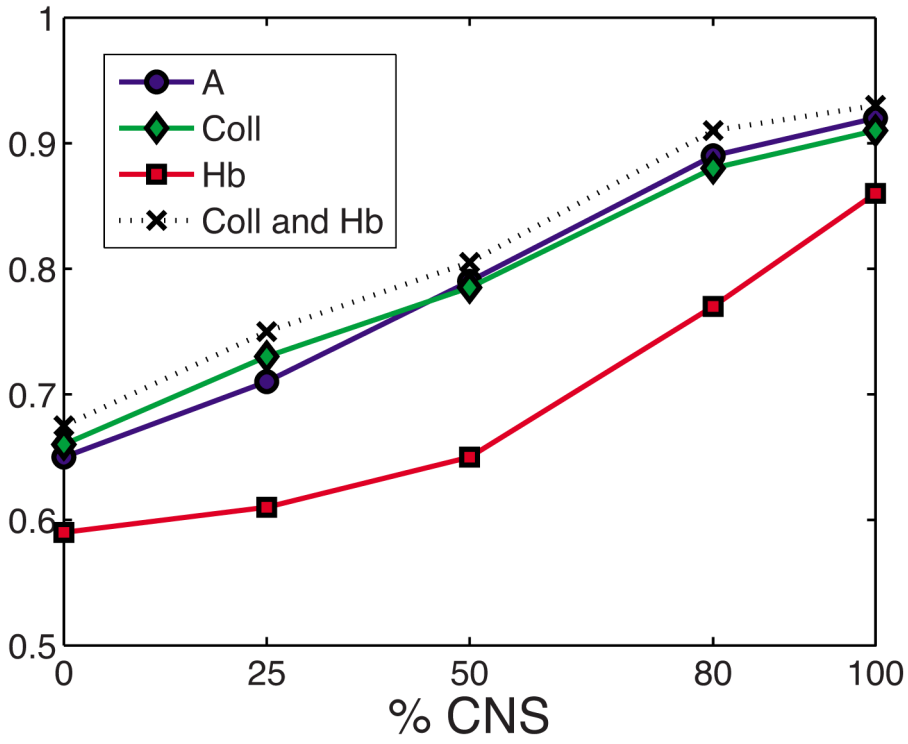

Fig. 4.

Area under the LCV ROC curve (AUC) for logistic regression models based on (1) *A* parameter (circles), (2) *Coll* (diamonds), (3) *Hb* (squares), and (4) *Coll* and *Hb* (crosses) as a function of percentage of CNS sites included in the data set.

Table 1

Contact probe data set.

Clinical category	Histology category		Number of sites
Normal (CNS)	Not biopsied		33
Suspicious	Non-HSIL	Negative for SIL	30
		LSIL	12
	HSIL		9

Table 2

Significant parameters for differentiating HSIL from negative sites (biopsied non-HSIL and CNS) as a function of the percentage of CNS sites included in the test sample.

CNS (% negative)	0%	25%	50%	80%	100%
Number of non-HSIL/Number of CNS	42/0	42/14	33/33	8/33	0/33
Significant parameters	*A, Hb, Coll*	*A, Hb, Coll*	*A, Hb, Coll, B*	*A, B, C, Hb, α, bvr Coll*	*A, B, C, Hb, α, bvr Coll*